# Elastohydrodynamic mechanisms govern beat pattern transitions in eukaryotic flagella

Shibani Veeraragavan[1], Farin Yazdan Parast[1], Reza Nosrati[1], Ranganathan Prabhakar[1,*]

[1] *Department of Mechanical and Aerospace Engineering, Monash University, Clayton, Victoria 3800, Australia*

## Abstract

Eukaryotic cilia and flagella exhibit complex beating patterns that vary depending on environmental conditions such as fluid viscosity[1]. These transitions are thought to arise from changes in the internal forcing provided by the axoneme, although the mechanism remains unclear[2,3]. We demonstrate with simulations of Kirchhoff rods driven internally by active bending moments that a single elastohydrodynamic instability universally explains transitions between planar, quasiplanar, helical, and complex beating patterns due to changes in either the internal forcing, flagellar stiffness and length, or due to changes in the hydrodynamic resistance, either due to the viscosity of the ambient medium or the presence of a plane wall. The beat patterns and transitions are comparable to those exhibited by bull sperm and sea urchin sperm in our experiments and elsewhere[3–5]. Our results point to a general model that can describe flagellar and ciliary beating across all species. We further show that internal dynein forces can be estimated by comparing simulation results with experimental observations of transitional viscosities. This can potentially lead to diagnostic assays to measure the health of sperm cells based on their beating pattern.

[*] prabhakar.ranganathan@monash.edu

## Introduction

The wavy motion of cilia and flagella is central to the biological function of many eukaryotic organisms[6,7]. These hair-like filaments are found both in free-swimming microorganisms, such as sperm or *Chlamydomonas*, as well as in ciliated cells within larger organisms such as the epithelial cells that line the reproductive tract and airways in mammals[7]. The regular beating of these filaments is powered by the axoneme. While the structure of this highly intricate internal "engine" has been studied extensively, many aspects of the mechanisms behind its operation are still not understood.[8]

In most eukaryotic species, the axoneme consists of nine interconnected microtubule doublets are arranged in a ring-like manner surrounding a central pair of microtubules[8]. This 9+2 structure is conserved across all eukaryotic species. Forces exerted by dynein motors situated between the doublets in the outer ring cause them to slide relative to each other. The seminal work of Julicher and Prost[9] further showed that the mechanism that generates the oscillations in flagella or cilia may also be universal: oscillations spontaneously arise as the result of a mechanical instability when a large number of motors act on elastic filaments.

Despite these shared features, swimming eukaryotic cells, particularly sperm display a remarkable diversity in flagellar beating patterns. For example, bull sperm flagella exhibit transitions from a three-dimensional (3D) rolling beat in bulk fluid to a two-dimensional (2D) planar beat when within a micrometre of a surface[10] which causes slithering motion along the surface. Sea urchin sperm also exhibit a quasi-planar beat close to a wall and 3D beating away from walls[3]. Planar beating is also observed when sperm swim in fluids of viscosity above around 20 mPa s.[4,5]

How does one explain these transitions observed in beating patterns? The travelling waveforms generated in the filaments could depend on the biochemical regulation of dynein motor activity, which in turn may modify the mechanism behind the oscillatory instability in the axoneme[11–18] or could modify the amplitude, wavelength and wave speed of the emergent travelling wave[19–24]. It would therefore seem that the variety in flagellar waveforms is largely due to internal differences in the dynein forcing.

We show here, however, that, like the origin of flagellar oscillations, transitions in beat patterns, may also be due to a *universal* elastohydrodynamic instability that does not require complex mechanosensing or biochemical regulation of the dynein activity. To do so, we model a flexible but inextensible elastic filament suspended in a viscous fluid. The filament is driven internally

by a travelling wave of active bending moments. That is, we take as given a mechanism that generates the internal forcing wave arising from the motor activity. Importantly, in every cross-section, the plane of the oscillation of the forcing wave is constant *relative to the material frame of reference associated with that cross-section*. The cross-sections can, however, rotate relative to each other as the filament when bends or twists.

We observe that increasing the fluid viscosity can trigger an abrupt transition from planar beating to helical beating and back. We also find that higher amplitude of the driving wave triggers a transition to helical beating. Our analysis suggests that these transitions are due to an elastohydrodynamic instability, indicating that 2D-to-3D transition in beating patterns can occur *generically* in sperm or cilia when the hydrodynamic resistance due to the ambient medium changes, either due to changes in the viscosity of the medium or due to the increased resistance while swimming near a wall. These observations are in good qualitative agreement with the observations of beat transitions in experiments by us (with bull sperm) and others[3–5] (with bull and sea-urchin sperm).

This study thus sheds light on how cilia and flagella could in general 'sense' and react to the hydrodynamic resistance of their surroundings. These results are relevant to both external and internal fertilization and suggest that sperm size of different species and other internal operating conditions within flagella may have evolved to ensure a planar beat in their natural environment. Defects in cilia and flagella such as an abnormal length or bending stiffness can greatly alter beating patterns and hence lead to poor swimming or to impaired function.

## Results

### 3D beating patterns emerge from internally planar oscillations in active bending moments.

We modelled a flagellum or cilium as an inextensible and unshearable but flexible filament (Kirchhoff rod[25]) suspended in a viscous Newtonian fluid (see Methods) [19,26]. The effect of motor activity was modeled by imposing a sinusoidal travelling wave in the active bending moment. We studied the effect of varying wavelength, frequency and amplitude of the imposed active wave on the motion state of the filament after thousands of forcing cycles. These driving parameters are expressed here in dimensionless terms as the wavenumber, $k$, the swimming number[27], $S = L(\omega\,\mu/K_B)^{1/4}$ and the amplitude ratio, $A = \alpha\, L/K_B$, where $L$ is the filament length, $K_B$ is its bending stiffness, $\mu$ is the viscosity of the suspending medium, and $\alpha$ and $\omega$

are the forcing amplitude and angular frequency, respectively. The swimming number is the ratio of the time scale of the passive elastohydrodynamic response of the system to $\omega^{-1}$, the time period of the forcing wave. The order of magnitudes for $S$ (from 2 to 21) and $A$ (from 5 to 30) were based on the beat frequencies and flagellar curvatures of sperm observed in our experiments. The wavenumber $k$ was set to either $2\pi$ or $4\pi$ to result in one or two forcing waves over the length of the filament, respectively. These correspond to the wavenumbers observed in bull and sea urchin (*Echinus esculentus*) sperm. In each case, we studied the distributions of the curvature $\kappa$ and the torsion $\tau$ along the filament length shapes after a large number ($10^3$) of forcing oscillations had been imposed. Proper Orthogonal Decomposition (POD) was used to resolve the curvature distribution into spatial modes and their respective time-dependent coefficients.[28] The power spectral densities (PSDs) of the first time-dependent POD coefficient of curvature were normalized by their peak values, and used to compare the periodicities in the observed beat patterns.

We uncovered four different types of beating patterns (Fig. 1 A-D) by comparing kymographs of the curvature (Fig. 1 E-H) and torsion functions (Fig. 1 I-L), and the curvature PSDs (Fig. 1 M-P). The imposed travelling wave in the active moment resulted in travelling waves emerging in curvature and torsion, as shown by the inclined bands in the kymographs. Since the oscillation in the imposed bending moment is always exerted about the same axis at each cross-section, the simplest response that we expect is *planar* beating characterized by the absence of torsion (Column underneath Fig. 1A; $S = 7, A = 5, k = 2\pi$; Supplementary Video 1). *However, we observed that torsion can spontaneously emerge in response to driving that is internally unidirectional.* We observed beating patterns that had banded torsional kymographs but with only a single frequency peak in the curvature PSDs (Column underneath Fig. 1B; $S = 5, A = 5, k = 2\pi$; Supplementary Video 2). When beating is perfectly planar, then the orientation of the beating plane remains fixed in space. Beat patterns with a simple travelling wave in torsion (Fig. 1B, F, J) resulted in a steady rolling of the beating plane of the filament; we therefore dub these beat patterns as *quasiplanar* states. In contrast, in *helical* beating (Column underneath Fig. 1C; $S = 12, A = 20, k = 4\pi$; Supplementary Video 3), a helical wave travels from the head towards the tail while the filament as a whole rolls over a cylindrical surface. Such beats had PSD peaks at the driving frequency as well as its harmonics with a more complex torsional structure. An interesting feature of the helical beating is that the filaments exhibited small vibrations superimposed over the helical shapes. We also observed

more *complex* 3D beats whose curvature PSDs included several harmonic as well as subharmonic peaks (Column underneath Fig. 1D; $S = 15, A = 20, k = 4\pi$; Supplementary Video 4).

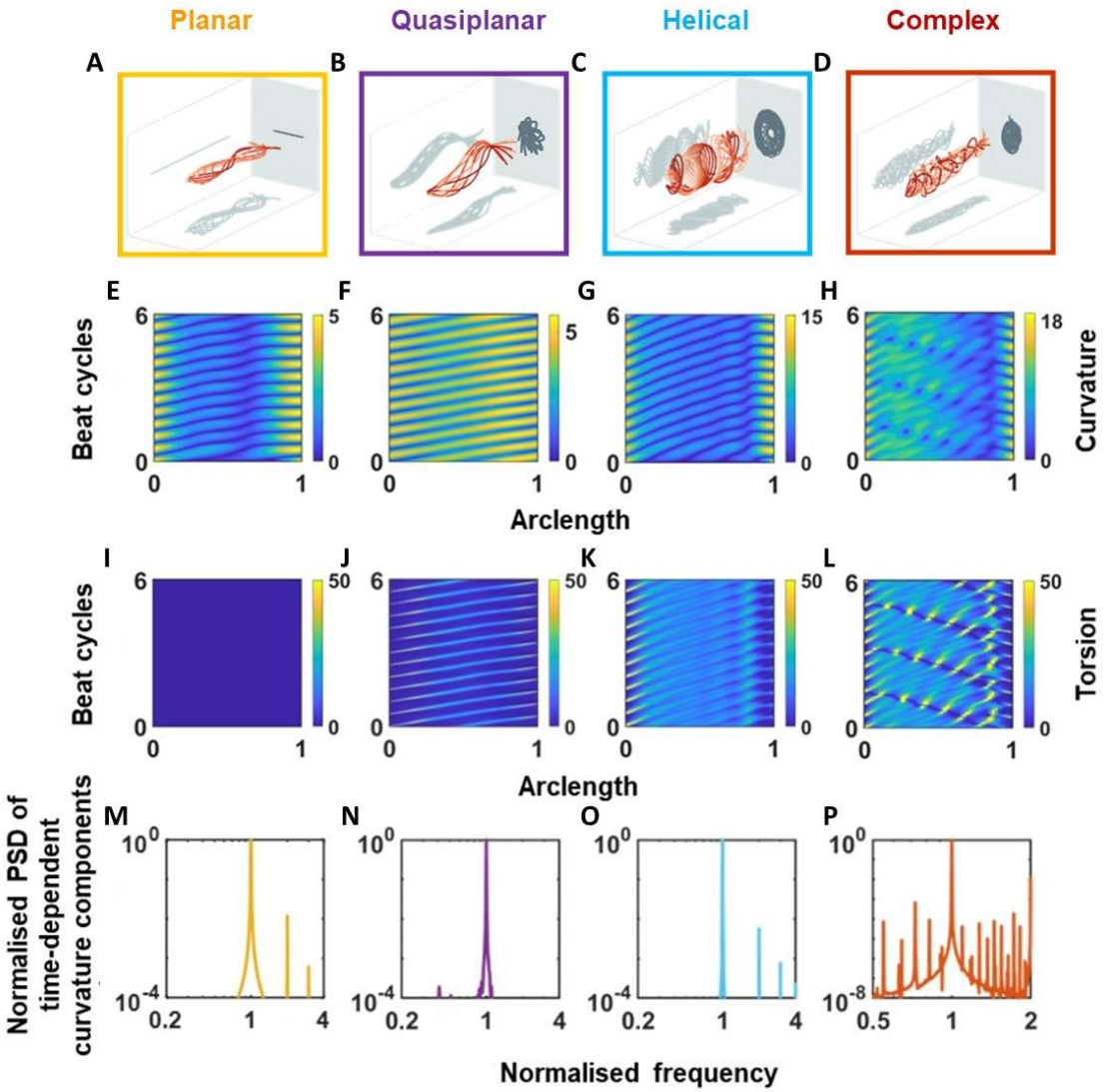


**Fig. 1 | Quantitative comparison of the four beating pattern types.** Representative images of the four qualitative beating types: (A) planar ($S = 7, A = 5, k = 2\pi$), (B) quasiplanar ($S = 5, A = 5, k = 2\pi$), (C) helical ($S = 12, A = 20, k = 4\pi$), (D) complex ($S = 15, A = 20, k = 4\pi$) beats. (E-H) Curvature kymographs, (I-L) torsion kymographs, and (M-P) normalised power spectral densities of the first time-dependent components of curvature for the representative planar ($S = 7, A = 5, k = 2\pi$), quasiplanar ($S = 5, A = 5, k = 2\pi$), helical ($S = 12, A = 15, k = 4\pi$) and complex ($S = 15, A = 20, k = 4\pi$) beats as labelled.

## 2D-3D beat transitions are correlated with changes in medium viscosity.

The beat patterns in our simulations resemble those observed in sperm. Planar beating has been observed in various species of mammalian sperm when viscosity is increased[4,29,30] or close to

surfaces[10,31] as well as in marine invertebrates such as sea urchin in standard saline[3,32]. The quasiplanar motion is seen in bull[4,5] and human sperm[30] swimming in low viscosity media (water-like viscosities, Supplementary Video 5) where the flagellum beats in a largely planar fashion and the beating plane rolls as the cell moves (Fig. 2B, H). Helical beating in sperm is well known[3], and vibrations in helical beats have also been observed in sea urchin sperm[3] swimming at 1500 mPa · s. Complex non-periodic beat patterns (as in Fig. 2D) have also been experimentally observed in pigeon sperm.[33]

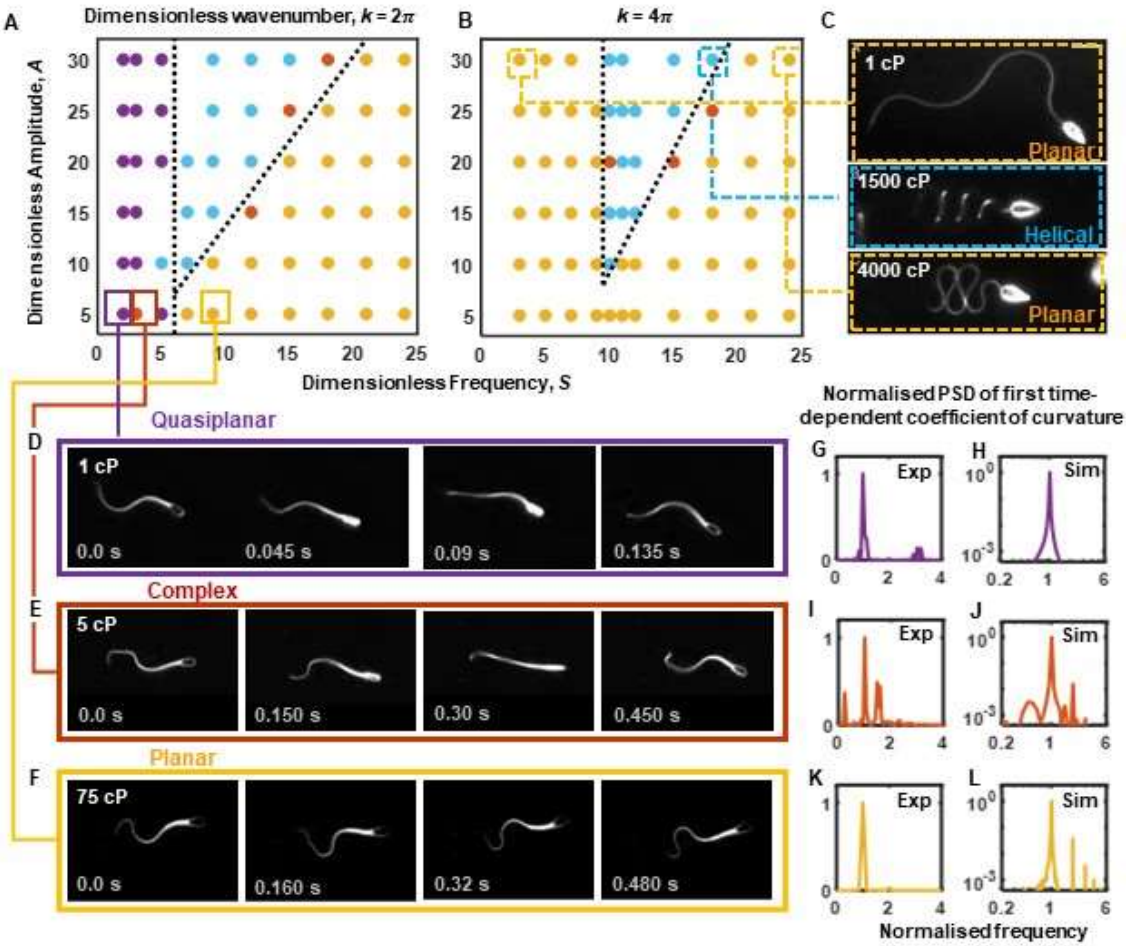


**Fig. 2 | Phase-maps of beating patterns and transitions between them.** Phase maps relating the different beating patterns to the amplitude ratio, *A* and the swimming number, *S*, for a wavenumber of (A) 2π and (B) 4π. The yellow, purple, blue and red symbols represent the planar, quasiplanar, helical and complex beat patterns. The dotted boundaries between the phase regimes are drawn to guide the eye. (C) Beat patterns of sea urchin sperm reported by Woolley and Vernon[3] at 1 cP (planar - top), 1500 cP (helical - middle) and 4000 cP (planar - bottom) linked to their equivalent datapoint in A. Timelapse images of bull sperm from our dark-field microscopy experiments indicating (D) quasiplanar, (E) complex and (F) planar beat observed in external medium viscosity of 1 cP, 5 cP and 75 cP, respectively. Power spectral density (PSD) of the first time-dependent coefficient of the projected 2D curvature from experimental data for (G) quasiplanar beat shown in D, (I) complex beat shown in E, and (K) planar beat shown in F, with the PSDs from our simulations in (H), (J), and (L), respectively.

These and other observations elsewhere[34] suggest a strong connection between beating patterns and medium viscosity.

Since the ratio $S$ depends on the viscosity $\mu$, to better understand how viscosity affects beating patterns at any given amplitude of the internal active wave, we have mapped in Fig. 2 the four kinds of beat patterns to the values of $A$ and $S$ in our simulations for each of the two values of the wavenumbers we studied. When $k = 2\pi$, distinct domains are observed in Fig. 2 E corresponding to quasiplanar (purple symbols), planar (yellow), and helical (blue) beats. For values of $S$ below 6, the beating pattern was predominantly quasiplanar, accompanied by rolling filament motions. In the region approximately bounded by the lines $S = 6$ and $A = 1.67S - 3$, the beat was predominantly helical. At all other values of $S$ and $A$, the beat was predominantly planar. The phase map is noticeably different at the higher wavenumber of 4π. Specifically, the quasiplanar beat was not observed, and the region of the map over which helical beating occurred diminished to between $S = 9$ and $A = 2.4S - 14.8$. At both $k = 2\pi$ and 4π, isolated instances of complex beating occurred at the boundaries between 3D and 2D beats for S and A values higher than 15 and 20, respectively.

**Elastohydrodynamics explains beat transitions across sperm species.**

We considered whether our simulation results are consistent with the experimental data of Woolley and Vernon[3] with sea urchin sperm (Fig. 2 C), and also our experimental observations with bull sperm (Fig. 2 D-F) swimming (see Methods). In an aqueous medium of 1 mPa·s, where sea urchin sperm exhibit planar beating (Fig. 2 C), bull sperm exhibited a rolling quasiplanar beat (Fig. 2 D and Supplementary Video 5). The rolling of the cell was observed in the videos as periodic flashes of high intensity in the head region (Supplementary Fig. 1 A). The quasiplanarity of the flagellum is also evident in the periodic oscillation of the projected length of the flagellum (Supplementary Fig. 1 B): the projected length drops is minimum (maximum) when the flagellar plane is perpendicular (parallel) to the focal plane. When the medium viscosity was increased to 1500 mPa·s and 4000 mPa·s, sea urchin sperm exhibited helical, and non-rolling planar beats (Fig. 2 C). In our experiments, on the other hand, when the viscosity was increased to 5 mPa·s, bull sperm exhibited a complex three-dimensional motion (Fig. 2E and Supplementary Video 6), whereas at 20 mPa·s, the beat was planar (Fig. 2F and Supplementary Video 7).

To determine the values of $S = L(\omega\,\mu\,/\,K_B)^{\frac{1}{4}}$ corresponding to the viscosities in the experiments, for sea urchin sperm[3], we used a flagellar length of 42 $\mu$m, a beat frequency of 50 Hz, and a bending stiffness of $1 \times 10^{-21}$Nm$^2$.[35] The values of $S$ corresponding to the viscosity values of 1 mPa·s (planar), 1500 mPa·s (helical) and 4000 mPa·s (planar) in the sea urchin experiments are 3, 18 and 24, respectively, while values for the bull sperm in our experiments, $S \approx 2$, 3 and 4 for viscosities of 1 cP (quasiplanar), 5 cP (complex) and 75 cP (planar), respectively. Calculation of the amplitude ratio $A = \alpha\, L/K_B$ requires the amplitude of the active moment wave, $\alpha$. Since this is not directly measurable in experiments, the approximate values of $A$ for the experimentally observed states were inferred as follows. We assumed that $\alpha$ remains unaffected by the external medium viscosity, only depending on the concentration of the other physiologically relevant medium constituents, which were not varied in the experiments considered here. This implies that the value of $A$ is a constant for each of the species. We then lined up the estimated values of $S$ for the observed motion states with the phase maps (Fig. 2 A with $k = 2\pi$ for bull sperm; Fig. 2 B with $k = 4\pi$ for sea urchin) to find the best values of $A \approx 5$ for bull sperm and 30 for sea urchin sperm. The PSDs of the curvatures of the 2D-projections in the microscope images (Fig. 2 G, I, K) were found to be qualitatively comparable with the PSDs of the first time-dependent POD coefficient of curvature in the simulations (Fig. 2 H, J, L) with the parameter values estimated as discussed above.

**Mechanical instability causes the emergence of 3D beat patterns.**

Our results above clearly demonstrate that even if the active bending moment in the axoneme always acts in the same plane in the local material reference frame associated with each cross section, the filament can develop torsion and the beating can become non-planar. Further, in the regions of the phase map in Fig. 2 A where the beating is 3D, the beating pattern quickly becomes non-planar from the straight-rod initial condition within a small (less $\lesssim 10$) number of beat cycles (Supplementary Figure 2). Our simulations fully accounted for the effect of the viscous flow generated around the filament through the Stokesian hydrodynamic-interaction tensors[36,37]. To understand whether the emergence of filament torsion is due to the complicated flow around the filament, we repeated our simulations by replacing the Stokesian Dynamics model with the simpler Resistive Force Theory (RFT) which ignores the effect of the flow generated around each segment by the motion of the other segments of the filament, and only retains the local anisotropic hydrodynamic resistance experienced by each segment of the slender filament.

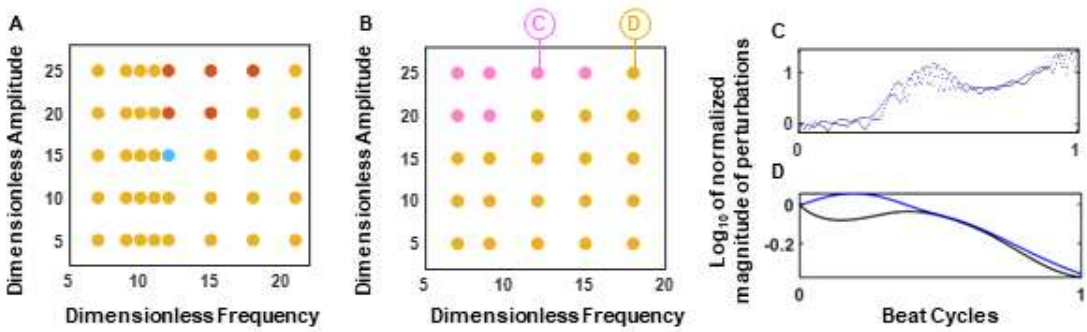


**Fig. 3 | Elastohydrodynamic origins of the three-dimensional beats at k = 4π.** (A) Phase map showing the emergence of planar (yellow), helical (blue) and complex (red) beating when considering only local anisotropic hydrodynamic drag. (B) Phase map showing points where out-of-plane shape perturbations decay (yellow, corresponding to planar beating) and grow (pink, corresponding to non-planar beating). $\text{Log}_{10}$ of the normalized magnitude ($L^2$ norm) of perturbations $\Omega_1$ (black) and $\Omega_2$ (blue) as a function of time (shown in terms of beat cycles) for (C) planar and (D) non-planar beating points indicated in (B).

We found that 3D beating still emerged (Fig. 3 A), although the range of parameters over which this behaviour was observed diminished to between $S = 11.5$ and $A = 1.68S - 7.37$, as opposed to between $S = 9$ and $A = 2.4S - 14.8$ in the model with the full non-local hydrodynamic interactions due to the flow around the filament. Interestingly, the 3D beat patterns obtained with RFT in Fig. 3 A are predominantly of the complex type, instead of the helical beats in Fig. 2 A and B.

The emergence of 3D beating while using RFT indicates that the non-planarity is not a result of the complex flow pattern driven around the beating filament. We next analysed the linear stability of the beat patterns in the RFT simulations. We first performed 2D simulations in which the equations for the $z$ coordinate of the filaments were ignored; that is, the filaments were constrained to two dimensions. The shape of the filament obtained after steady beating had been achieved was used as the initial condition for a separate simulation of the linearized 3D equations for the evolution of a small out-of-plane perturbation. Noting that a planar beat only has a non-zero curvature along one material direction $\mathbf{d}_3$ (corresponding to the generalized curvature $\Omega_3$; see Methods), an out-of-plane perturbation consists of a combination of perturbations along the other two material directions. If, for a given combination of $S$ and $A$, such a perturbation grows in amplitude with each successive beat cycle (e.g. Fig. 3 C), it indicates that the planar beating state for that parameter combination is unstable to small perturbation in full 3D simulations. On the other hand, if the initial perturbation continuously decays in magnitude (e.g. Fig. 3 D), the planar beat is stable. The results in Fig. 3 B indicate that the transition observed with the full 3D RFT simulation in Fig. 3 A as $A$ increases for $S = 12$ and 15 as well as the transition from three-dimensional to planar beating as dimensionless

frequency increases from $S = 15$ to 18 at $A = 25$ is due to the linear elastohydrodynamic instability of planar beating. However, the stability of planar beats at $S \leq 11$ and $A \geq 20$ is not captured in Fig. 3 B. Further, the onset of three-dimensional beating in Fig. 3 A occurs at lower values of $A$ than predicted by the stability analysis. This suggests that nonlinear effects have both stabilizing as well as non-stabilizing influences[24].

**Beat patterns are strongly modified by flow near surfaces.**

Overall, the results in the sections above clearly show that the experimentally-observed 2D-3D beating transitions in sperm are likely to be universally observable in any eucaryotic cilia or flagella, if the viscosities of the ambient fluid are such that the operating conditions span the phase boundaries in Fig. 2. The proximity of a no-slip surface also increases the hydrodynamic resistance encountered by a swimming cell. Experimentally, there is clear evidence that beating patterns are altered by the presence of walls.[38] With sea urchin sperm,[3] a transition from planar to quasi-planar beating (that appeared like a 'flattened' helical beat) was reported when moving away from the surface.

Incorporating Stokesian wall hydrodynamic-interaction tensors in our 3D simulations, we found that a filament that exhibits steady planar beating in bulk can become quasiplanar when it is at a distance of around 20% its length ($L$) from an infinite plane wall. For example, when $S = 9$, $A = 12$, $k = 4\pi$, a filament that was initially oriented parallel to the wall at $1.5\,L$ from the wall, was drawn towards the wall due to hydrodynamic attraction[39] (Fig. 4 A). The beating pattern initially remains planar with a slight 1° tilt towards the wall (top inset in Fig. 4 A). The filament then proceeds to accumulate at a distance of approximately $0.18\,L$ from the wall ($\sim 8\,\mu$m for sea urchin sperm and $\sim 15\,\mu$m for bull and human sperm) and switches to a quasiplanar beat (bottom inset of Fig. 4 A). The PSD of the curvature function (Fig. 4 B) shows that this near-wall quasiplanar beat is markedly different from the quasiplanar beat in bulk fluid (Fig. 2 L). Notably, the torsion profile shows a change in direction every few beat cycles (Fig. 4 C), which corresponds to changes in the rolling direction from clockwise to counterclockwise before the roll is fully completed. This quasiplanar beat is similar to that observed in sea urchin sperm[3], where the cell rolls slightly from one side to another without exhibiting complete rolls in either direction.

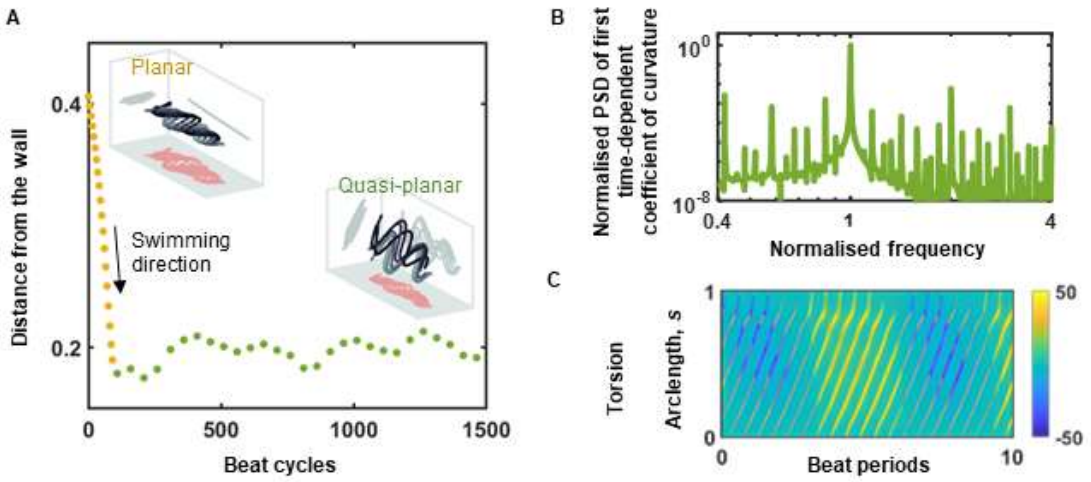


**Fig. 4 | Transition to quasi-planar beating near a plane wall.** (A) Head trajectory of an originally planar swimmer ($S$ = 9, $A$ = 12, $k$ = 4π) near a wall, with a transition from a planar beat (top) to a quasiplanar beat (bottom). Yellow points denote planar beating and green points denote quasiplanar beating. (B) Normalised power spectral density of the first time-dependent coefficient of curvature in a quasiplanar beat. (C) Kymograph of the spatiotemporal evolution of centerline torsion in a quasiplanar beat.

No such changes were observed in simulations using RFT with resistance coefficients modified to account for the distance from the wall[40], indicating that near-wall changes in beating patterns a result of the complex fluid flow close to a wall.

## Discussion

The origin of non-planar beating patterns in eucaryotic cilia and flagella has been a long-standing mystery. It has been shown that spatiotemporal oscillations will spontaneously arise when motors act on elastic elements[9]. This basic mechanism can be further augmented by the regulation of the motors[17,41–43]. Indeed, detailed experimental investigation of the states of the dynein motors has revealed that motors on one side of the doublet ring are inhibited at any time at each cross section.[44] These experiments also show that motors are switch-inhibited in an oscillatory manner as the bending wave propagates down the filament. These observations lend support to the idea that the wave of active bending moment generated collectively by the motors is internally planar. On the other hand, there is considerable experimental evidence that cilia and flagella exhibit both planar and non-planar beating patterns. To explain non-planar beating, more complex 3D regulation of motor activity has been suggested. [2,3,45,46] However, transitions between 2D and 3D beating are observed in a single species when the environmental conditions

change. Explaining such transitions becomes challenging with mechanisms for 3D beat pattern generation that are purely based on motor regulation.

Our results instead show that 3D beating and 2D-3D beat transitions may have a simpler elastohydrodynamic origin that is generic to all eucaryotic species. This is in tune with the fact that the axoneme structure is highly conserved across eucaryotic species and that the underlying mechanisms that give rise to spontaneous bending-moment oscillations are also generic. The 3D wave patterns generated by this universal mechanism can capture the rolling quasiplanar, helical, and more irregular beat patterns that have been observed in experiments. The results here moreover clearly show how the beating patterns are related to the length and stiffness of the ciliary or flagellar filament, the oscillatory characteristics of the active bending wave, as well as the hydrodynamic properties of the ambient medium. We have shown that the variety of beating patterns due to changes in the ambient medium viscosity can be systematically predicted with a single model.

This work is in line with recent work that has underscored the importance of mechanical instabilities in understanding the shapes and dynamics of cilia and flagella[13,14,16,18,22,24,47–52]. Gadêlha *et al.*[24] demonstrated that asymmetric beating in planar internally-driven filaments can occur due to buckling instabilities, and do not require any morphological asymmetry or asymmetry in internal forces. This work extends their findings to the emergence of three-dimensional asymmetrical beating without internal asymmetries. Our results also confirm findings there and elsewhere[18] that nonlinear effects become important at parameters that induce high flagellar curvatures. Rode *et al.*[22] and Ling *et al.*[47] showed that mechanical instabilities can lead to transitions between planar and three-dimensional beating for different types of internal driving patterns. Both these studies, focused on changes in the internal driving parameters such as, for example, the wavelength of the active bending moment in Rode *et al* [22]. A purely internal mechanism for viscosity-related transitions would require some additional mechanosensory processes to couple the internal forcing to the ambient viscosity. Our results here show instead that viscosity-related beat transitions in sperm could occur even without any such complex internal regulation of the dynein forcing.

The observation that three-dimensional waveforms emerge from internally planar driving even when the hydrodynamic drag is modeled by the Resistive Force Theory is of interest to other systems involving the inertialess locomotion of elastic filaments experiencing anisotropic local frictional resistance – for example, the motion of snake-like organisms or robots within dry granular media[53]. Beyond that, the differences between the simulation results and with (Fig.

2B) and without (Fig. 3A) show that long-range hydrodynamic interactions significantly modify the waveforms that develop after it emerges due to the instability. Our observations further show that these interactions are even more important in determining beating patterns in the presence of confining surfaces.

We have demonstrated that the transitional viscosity values at which beating patterns change from planar to quasiplanar and back can be matched with simulation results to extract the dimensionless active moment amplitude, $A$. This value can further be related to the average force exerted by a dynein motor in the axoneme. Since the active moment amplitude generated by the dynein motors in the cross-sectional reference frame is $\alpha k$ (see Methods), the force per dynein motor is estimated as $A\, K_B\, k/(2\, n\, r\, L)$ , where $r$ is the radius of the axoneme, and $n$ is the number of dyneins per unit length. For sea urchin sperm, with a value of $A = 30$ estimated by matching of the transitional viscosities with simulation results, and $r = 80$ nm[54] and $n = 198$ [55,56], we obtain an average force per motor of 6.6 pN. Similarly, for bull sperm, $A = 5$ yields 0.9 pN per motor. These values are comparable to the experimentally measured range of $2 - 5$ pN per dynein[56].

The analysis above suggests that it is possible to exploit measurements of viscosities at which 2D-3D transitions in beat patterns to extract quantitative estimates of internal forcing. Recently, a microfluidic device was used to systematically study the effect of varying viscosity on the flagellar waveforms of single sperm cells[57]. Transitional viscosities obtained in such devices could be combined with independent measurements of the bending stiffness and compared with results from detailed simulations that account for features that have been neglected here (*e.g.* nonuniformity in filament radius due to the head and the flagellar taper, weak viscoelasticity induced by the methylcellulose viscosifier, *etc.*) to yield more accurate values of dynein forcing. Such assays can study the effect of signalling molecules or ionic species on motor forcing, thus enabling the construction of detailed models of the biochemical regulation of the axoneme. Measurements of the response of dynein forcing to biochemical signals could also have diagnostic applications.

Interestingly, our experiments showed that, despite the wavenumber differences between sea urchin sperm and bull sperm, planar beating is exhibited by the former at low viscosities, and high viscosities by the latter. The corresponding estimates of the dynein forces were different in the two species, as are their lengths. It is possible that the values of these parameters are selected by evolution to enable planar beating in the viscosities of their natural environments. Since the dependence of $S$ on viscosity is weak ($\sim \mu^{\frac{1}{4}}$), if sperm of a given species operate

sufficiently far from helical-planar transition, its natural beating pattern could be robust to large changes in the viscosity of the ambient fluid. On the other hand, if the operating point is close to the boundary, then small variations in length, morphology or axonemal characteristics between individual sperm could yield significantly different beating patterns even within the population of sperm in a single semen sample[4,5]. The parameter $A$ is directly proportional to the dynein forcing; hence, biochemically-mediated changes to motor forces can cause the operating point to change in the vertical direction and cross the helical-planar boundary to effect a change in beat pattern and swimming trajectory. The implications of such changes to the overall energetics and propulsion efficiency remain to be explored.

## Methods

### Model for the flagellum

At any with instant of time $t$ the position and shape of the filament is characterized by the centerline position vector distribution, $\mathbf{r}(s,t)$, where $s$ is the arclength coordinate along the centerline of the inextensible filament. The orientation of every cross-section is characterized by the triad of orthogonal unit vectors formed by the unit tangent vector,

$$\mathbf{d}_1 = \frac{\partial \mathbf{r}}{\partial s}, \tag{1}$$

and the unit vectors, $\mathbf{d}_2$ and $\mathbf{d}_3$ that lie in the plane of the cross-section (Fig. 5). These material frame vectors related to each other such that

$$\frac{\partial \mathbf{d}_i}{\partial s} = \Omega \times \mathbf{d}_i, \tag{2}$$

where the components of the $\Omega$ vector are the generalized curvatures that describe how quickly the material reference frame rotates as one travels down the filament, at any given instant of time[58].

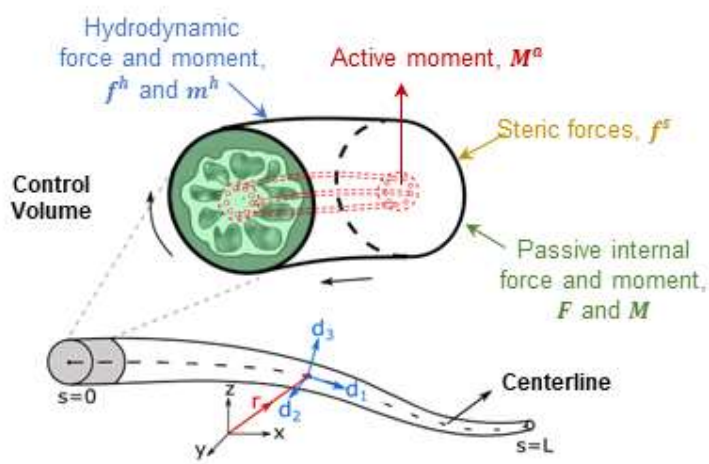


**Fig. 4 | The internally-driven Kirchhoff-rod model.**

The kinematics of the inextensible filament are given by:

$$\frac{\partial \mathbf{r}}{\partial t} = \mathbf{v}, \tag{3}$$

$$\frac{\partial \mathbf{d}_i}{\partial t} = \mathbf{w} \times \mathbf{d}_i, \tag{4}$$

where $\mathbf{v}$ and $\mathbf{w}$ are the translational and rotational velocities of the rigid cross sections, respectively. Any differential control volume experiences external hydrodynamic forces and

torques, and passive internal forces and moments due to elasticity that resist stretching, bending and twisting. In the absence of any external forces, and when inertial effects are negligible, conservation of linear momentum yields[26,59]:

$$\frac{\partial \mathbf{F}}{\partial s} + \mathbf{f}^{\mathrm{h}} + \mathbf{f}^{\mathrm{s}} = \mathbf{0}, \tag{5}$$

where $\mathbf{F}$ is the internal tension force exerted on a cross-section by the material on its aft side, and $\mathbf{f}^{\mathrm{h}}$ and $\mathbf{f}^{\mathrm{s}}$ are the hydrodynamic and steric forces per unit length. The steric excluded-volume force was implemented as in Schoeller *et al*.[60] Angular momentum conservation leads to[26,59]

$$\frac{\partial \mathbf{M}}{\partial s} + \mathbf{d}_1 \times \mathbf{F} + \mathbf{m}^{\mathrm{h}} + \frac{\partial \mathbf{M}^{\mathrm{a}}}{\partial s} = \mathbf{0}, \tag{6}$$

where $\mathbf{m}^{\mathrm{h}}$ is the hydrodynamic moment per unit length. For a filament with no intrinsic curvature, the elastic bending moment at each cross-section is:

$$\mathbf{M} = K_B \left( \frac{\partial \mathbf{d}_3}{\partial s} \cdot \mathbf{d}_1 \, \mathbf{d}_2 + \frac{\partial \mathbf{d}_1}{\partial s} \cdot \mathbf{d}_2 \, \mathbf{d}_3 \right) + K_T \frac{\partial \mathbf{d}_2}{\partial s} \cdot \mathbf{d}_3 \, \mathbf{d}_1, \tag{7}$$

where $K_B$ and $K_T$ are bending and twisting stiffness coefficients, respectively. The effect of the axonemal driving is modeled as a travelling wave of active moment always acting about the binormal direction at every cross-section:

$$\mathbf{M}^{\mathrm{a}} = \alpha \sin(k\, s - \omega\, t)\, \mathbf{d}_3, \tag{8}$$

where $\alpha$, $k$ and $\omega$ are the amplitude, wavenumber and frequency of the travelling wave. This driving moment is equivalent to imposing a travelling preferred-curvature wave in $\Omega_3$. The oscillating active moment at each cross-section is thus always exerted about the same axis in the material frame associated with that cross section. If the filament shape is always planar with respect to the global laboratory-attached reference frame, then the driving moment above will also be planar in the global reference frame. However, the kinematics and dynamics described by the set of model equations above do not constrain the filament to remain planar, and it is possible that the filament takes a non-planar shape in the global frame in response to the locally-unidirectional active internal moment.

The relationship between the hydrodynamic force and moment and the linear and angular velocity at each cross section were expressed in terms of hydrodynamic mobility matrices as:

$$\begin{bmatrix} \mathbf{v}\,(s,t) \\ \mathbf{w}(s,t) \end{bmatrix} = \int_0^L \begin{bmatrix} \mathcal{M}^{tt}(s,s') & \mathcal{M}^{tr}(s,s') \\ \mathcal{M}^{rt}(s,s') & \mathcal{M}^{rr}(s,s') \end{bmatrix} \cdot \begin{bmatrix} \mathbf{f}^{\mathrm{h}}(s',t) \\ \mathbf{m}^{\mathrm{h}}(s',t) \end{bmatrix} ds' \tag{9}$$

where $\mathcal{M}^{tt}$, $\mathcal{M}^{tr}$, $\mathcal{M}^{rt}$ and $\mathcal{M}^{rr}$ are mobility matrices that depend on the hydrodynamic model chosen. For filaments in an infinite viscous medium, long-range hydrodynamic interaction

between different segments along the filament were modelled using the Rotne-Prager-Yamakawa mobility tensors,[36,61] the tensors provided by Swan and Brady[37] were used to model filaments near an infinite plane wall after ignoring lubrication effects. We also used Resistive Force Theory with the drag coefficients provided by Lighthill[62] for free space and coefficients by Katz *et al.*[40] near a wall. The forms of these mobility matrices are available in the Supplementary Text.

We used the numerical method suggested by Schoeller *et al.* [60] to integrate the equations above forward in time until a steady oscillatory state was obtained. The material frame vectors were represented by unit quaternions to ensure that the vectors remain of unit magnitude at every time step, thus, satisfying the constraints that the filament is inextensible and cross-sections remain planar. An implicit second-order backward difference scheme was used to discretize the equations. Starting from a perfectly straight filament with $\mathbf{d}_i$ aligned with the unit vectors of the global reference frame, the quasi-Newton Broyden's method was used to iteratively solve the nonlinear system of equations to calculate the internal tension $\mathbf{F}$ enforcing the inextensibility constraint, and $\mathbf{f}^{\mathrm{h}}$ and $\mathbf{m}^{\mathrm{h}}$ from the known shape at each time step. These were then used in Eqn. 9 to calculate the velocities, and then the translational and angular displacements at the end of that time step.

We used $1/\omega$, $L$, and $K_B/L^2$ as the time, length, and force scales, respectively. The wavenumber of the forcing wave, $k$ was set to either $2\pi$ or $4\pi$ to match experimental observations in bull and sea urchin. The swimming number, $S$, was varied between 2 and 21. The dimensionless active moment amplitude, $A$, was varied between 5 and 30. The ratio of bending and twisting stiffnesses, $K_B/K_T$, was set to 1 and the dimensionless steric force parameter was set to a large value ($10^2$). The filament was subjected to force- and moment-free boundary conditions and was discretized into $N = 50$ segments of dimensionless length $\Delta s = 0.02$ and radius $a = 0.01$ units. This gives a radius-to-length ratio of 1/100, which approximately corresponds to that seen in various species of mammalian sperm, considering the radius of the thickest part of the flagellum.[63]

**Analysis of beat patterns**

We study shape changes using the Frenet curvature $\kappa(s,t)$ and torsion $\tau(s,t)$. The describes the local bending of the filament around any point, while the torsion describes the rate at which the centerline develops nonplanarity locally as it moves out of local bending plane. These

quantities remain invariant under any translation or rotation of the reference frame, and are defined as:

$$\kappa = \frac{\partial \mathbf{t}}{\partial s} \cdot \mathbf{n}; \qquad \tau = -\frac{\partial \mathbf{b}}{\partial s} \cdot \mathbf{n}, \tag{10}$$

where $\mathbf{t} = \mathbf{d}_1$, and $\mathbf{n}$ and $\mathbf{b}$ are the normal and binormal vectors, defined as:

$$\mathbf{n} = \frac{\partial \mathbf{t} / \partial s}{\|\partial \mathbf{t} / \partial s\|}; \quad \mathbf{b} = \mathbf{t} \times \mathbf{n}. \tag{11}$$

**Linear Stability Analysis**

For generating oscillating planar base-states, only two of the material frame vectors change with time, and the shape of the filament was described by a single variable $\theta(s,t)$, such that for a filament beating in the x−y plane:

$$\mathbf{d}_1 = \cos\theta\, \mathbf{e_x} + \sin\theta\, \mathbf{e_y};\ \mathbf{d}_2 = -\sin\theta\, \mathbf{e_x} + \cos\theta\, \mathbf{e_y};\ \mathbf{d}_3 = \mathbf{e_z}. \tag{12}$$

With this, the out-of-plane components of the translational velocities and forces are zero $\mathbf{d_1}$ while angular velocities and torques have a component only in the $\mathbf{d_3}$ direction. The hydrodynamic force and moment are

$$\mathbf{f^h} = -\zeta_1 v_1 \mathbf{d}_1 - \zeta_2 v_2 \mathbf{d}_2;\ \mathbf{m^h} = -\zeta_r \omega_r \mathbf{d}_3, \tag{13}$$

with the RFT drag coefficients are as shown in Eq. **Error! Reference source not found.**. Since $\Omega_3$ is the only non-zero curvature component,

$$\mathbf{M} = K_B \Omega_3\, \mathbf{e_z}\,. \tag{14}$$

The system was numerically integrated in time using the numerical algorithm described in Schoeller *et al.*[60] to obtain the planar base states at required parameters.

To explore whether the planar base states predicted by the simulations above are linearly stable to perturbations in the shape, the model equations were recast in terms of the evolution of curvature as follows (see Supplementary Text):

$$\frac{\partial}{\partial s}\left(\mathcal{M}^{tt} \cdot \frac{\partial \mathbf{F}}{\partial s}\right) = \mathcal{M}^{rr} \cdot \left[\frac{\partial(\mathbf{K}\cdot\mathbf{\Omega})}{\partial s} + \mathbf{d}_1 \times \mathbf{F} + \frac{\partial \mathbf{M}^{\mathrm{a}}}{\partial s}\right] \times \mathbf{d}_1 \tag{15}$$

$$\frac{\partial \mathbf{\Omega}}{\partial t} = \mathcal{M}^{rr} \cdot \left[\begin{array}{l} \frac{\partial}{\partial s}\left(\frac{\partial(\mathbf{K}\cdot\mathbf{\Omega})}{\partial s} + \mathbf{d}_1 \times \mathbf{F} + \frac{\partial \mathbf{M}^{\mathrm{a}}}{\partial s}\right) \\ + \left(\frac{\partial(\mathbf{K}\cdot\mathbf{\Omega})}{\partial s} + \mathbf{d}_1 \times \mathbf{F} + \frac{\partial \mathbf{M}^{\mathrm{a}}}{\partial s}\right) \times \mathbf{\Omega} \end{array}\right]. \tag{16}$$

The curvature and internal stress were expanded as $\mathbf{\Omega} = \mathbf{\Omega}^{(0)} + \mathbf{\Omega}^{(1)} + \cdots$ and $\mathbf{F} = \mathbf{F}^{(0)} + \mathbf{F}^{(1)} + \cdots$, where $\mathbf{\Omega}^{(0)}$ and $\mathbf{F}^{(0)}$ are the base-state curvature and internal tension predicted by the planar simulations, and $\mathbf{\Omega}^{(1)}$ and $\mathbf{F}^{(1)}$ represent leading order perturbations about the base state. By substituting these into Eqs. 15 and 16 and retaining terms only up to first order, we obtained the linearized scalar equations governing the evolution of the perturbation variables (see Supplementary Text). The perturbation variables were set to zero at the ends of the filament. We solved the system of equations over $s$everal beat cycles using the MATLAB PDE solver pdepe, starting with an initial sinusoidal perturbation in both $\Omega_1$ and $\Omega_2$:

$$\Omega_1^{(1)}(s,0) = \Omega_2^{(1)}(s,0) = \sin(\pi s) + \sin(2\pi s) + \sin(4\pi s) + g(s), \qquad (17)$$

where $g(s)$ represents a random number between −0.5 and 0.5.

**Sperm Sample Preparation and Imaging**

Bull semen were purchased from ABS Australia in $150\mu L$ straws and stored in liquid nitrogen prior to use. The semen samples were thawed in a 37°C water bath and diluted in a pre-warmed HEPES buffer (117 mM NaCl, 5.3 mM KCl, 1.8 mM $CaCl_2.2H_2O$, 0.8mM $MgSO_4$, 1mM $NaH_2PO_4$, 5.5 mM D-Glucose, 0.03 mM Phenol Red, 4 mM $NaHCO_3$, 21 mM HEPES, 0.33 mM Na Pyruvate, 21.4 mM Na Lactate, 0.3 mg/mL Bovine Serum Albumin and pH=7.4) supplemented with 0.1, 0.25 and 0.75% methylcellulose (M0512, Sigma-Aldrich) corresponding to a nominal viscosity of 1 cP, 5 cP and 75 cP, respectively. Diluted sperm samples were incubated at 37°C until imaging. To image bull sperm, $20\mu L$ of the prepared sperm sample were added to a chamber on a microscope slide, and then free-swimming sperm were imaged using high-speed high-resolution darkfield microscopy at 200 frames per second for 3 seconds. Imaging was performed using an AX-70 upright microscope (Olympus, Japan) equipped with an ORCA-Flash4.0 v2 sCMOS camera (Hamamatsu, Japan), a darkfield condenser (numerical aperture (NA)=0.9), and a U-DFA 18 mm internal diameter dark-field annulus with a UPlanAPO 10× magnification objective (NA= 0.4, Olympus, Japan). The sperm flagellar centreline was extracted using an automated image analysis algorithm as detailed in Nandagiri *et al.*[26]

## Data availability

All relevant data supporting the findings of this study are available within the article and its Supplementary Information files or upon request from the corresponding authors.

## Code availability

MATLAB code used to perform the simulations are available at https://doi.org/10.26180/21204512.v1.

## References


1. Gaffney, E. A., Gadêlha, H., Smith, D. J., Blake, J. R. & Kirkman-Brown, J. C. Mammalian Sperm Motility: Observation and Theory. *Annu Rev Fluid Mech* **43**, 501–528 (2011).

2. Lindemann, C. B. & Lesich, K. A. The many modes of flagellar and ciliary beating: Insights from a physical analysis. *Cytoskeleton* **78**, 36–51 (2021).

3. Woolley, D. M. & Vernon, G. G. A study of helical and planar waves on sea urchin sperm flagella, with a theory of how they are generated. *Journal of Experimental Biology* **204**, 1333–1345 (2001).

4. Zaferani, M., Javi, F., Mokhtare, A., Li, P. & Abbaspourrad, A. Rolling controls sperm navigation in response to the dynamic rheological properties of the environment. *Elife* **10**, (2021).

5. Hyakutake, T., Suzuki, H. & Yamamoto, S. Effect of viscosity on motion characteristics of bovine sperm. *Journal of Aero Aqua Bio-mechanisms* **4**, 63–70 (2015).

6. Badano, J. L., Mitsuma, N., Beales, P. L. & Katsanis, N. The Ciliopathies: An Emerging Class of Human Genetic Disorders. *Annu Rev Genomics Hum Genet* **7**, 125–148 (2006).

7. Konno, A., Setou, M. & Ikegami, K. Ciliary and Flagellar Structure and Function—Their Regulations by Posttranslational Modifications of Axonemal Tubulin. in *International Review of Cell and Molecular Biology* vol. 294 133–170 (Elsevier Inc., 2012).

8. Satir, P., Heuser, T. & Sale, W. S. A Structural Basis for How Motile Cilia Beat. *Bioscience* **64**, 1073–1083 (2014).

9. Jülicher, F. & Prost, J. Spontaneous Oscillations of Collective Molecular Motors. *Phys Rev Lett* **78**, 4510–4513 (1997).

10. Nosrati, R., Driouchi, A., Yip, C. M. & Sinton, D. Two-dimensional slither swimming of sperm within a micrometre of a surface. *Nat Commun* **6**, 8703 (2015).

11. Sartori, P., Geyer, V. F., Scholich, A., Jülicher, F. & Howard, J. Dynamic curvature regulation accounts for the symmetric and asymmetric beats of Chlamydomonas flagella. *Elife* **5**, (2016).

12. Brokaw, C. J. Computer Simulation of Flagellar Movement. *Biophys J* **12**, 564–586 (1972).

13. Oriola, D., Gadêlha, H. & Casademunt, J. Nonlinear amplitude dynamics in flagellar beating. *R Soc Open Sci* **4**, 160698 (2017).

14. Chakrabarti, B. & Saintillan, D. Spontaneous oscillations, beating patterns, and hydrodynamics of active microfilaments. *Phys Rev Fluids* **4**, 43102 (2019).

15. Riedel-Kruse, I. H., Hilfinger, A., Howard, J. & Jülicher, F. How molecular motors shape the flagellar beat. *HFSP J* **1**, 192–208 (2007).

16. Bayly, P. V. & Wilson, K. S. Equations of Interdoublet Separation during Flagella Motion Reveal Mechanisms of Wave Propagation and Instability. *Biophys J* **107**, 1756–1772 (2014).

17. Camalet, S. & Jülicher, F. Generic aspects of axonemal beating. *New J Phys* **2**, 324 (2000).

18. Li, C., Chakrabarti, B., Castilla, P., Mahajan, A. & Saintillan, D. Chemomechanical model of sperm locomotion reveals two modes of swimming. *Phys Rev Fluids* **8**, 113102 (2023).

19. Olson, S. D., Lim, S. & Cortez, R. Modeling the dynamics of an elastic rod with intrinsic curvature and twist using a regularized Stokes formulation. *J Comput Phys* **238**, 169–187 (2013).

20. Carichino, L. & Olson, S. D. Emergent three-dimensional sperm motility: coupling calcium dynamics and preferred curvature in a Kirchhoff rod model. *Math Med Biol* **36**, 439–469 (2019).

21. Simons, J., Olson, S., Cortez, R. & Fauci, L. The dynamics of sperm detachment from epithelium in a coupled fluid-biochemical model of hyperactivated motility. *J Theor Biol* **354**, 81–94 (2014).

22. Rode, S., Elgeti, J. & Gompper, G. Sperm motility in modulated microchannels. *New J Phys* **21**, 13016 (2019).

23. Ishimoto, K. & Gaffney, E. A. An elastohydrodynamical simulation study of filament and spermatozoan swimming driven by internal couples. *IMA J Appl Math* **83**, 655–679 (2018).

24. Gadêlha, H., Gaffney, E. A., Smith, D. J. & Kirkman-Brown, J. C. Nonlinear instability in flagellar dynamics: a novel modulation mechanism in sperm migration? *J R Soc Interface* **7**, 1689–1697 (2010).

25. Dill, E. H. Kirchhoff's theory of rods. *Arch Hist Exact Sci* **44**, 1–23 (1992).

26. Nandagiri, A. *et al.* Flagellar energetics from high-resolution imaging of beating patterns in tethered mouse sperm. *Elife* **10**, (2021).

27. Hall-McNair, A. L., Montenegro-Johnson, T. D., Gadêlha, H., Smith, D. J. & Gallagher, M. T. Efficient implementation of elastohydrodynamics via integral operators. *Phys Rev Fluids* **4**, 113101 (2019).

28. Werner, S., Rink, J. C., Riedel-Kruse, I. H. & Friedrich, B. M. Shape Mode Analysis Exposes Movement Patterns in Biology: Flagella and Flatworms as Case Studies. *PLoS One* **9**, e113083 (2014).

29. Ishimoto, K., Gadêlha, H., Gaffney, E. A., Smith, D. J. & Kirkman-Brown, J. Human sperm swimming in a high viscosity mucus analogue. *J Theor Biol* **446**, 1–10 (2018).

30. Smith, D. J., Gaffney, E. A., Gadêlha, H., Kapur, N. & Kirkman-Brown, J. C. Bend propagation in the flagella of migrating human sperm, and its modulation by viscosity. *Cell Motil* **66**, 220–236 (2009).

31. Friedrich, B. M., Riedel-Kruse, I. H., Howard, J. & Jülicher, F. High-precision tracking of sperm swimming fine structure provides strong test of resistive force theory. *Journal of Experimental Biology* **213**, 1226–1234 (2010).

32. Gong, A. *et al.* Reconstruction of the three-dimensional beat pattern underlying swimming behaviors of sperm. *The European Physical Journal E* **44**, 87 (2021).

33. Vernon, G. G. & Woolley, D. M. Three-dimensional motion of avian spermatozoa. *Cell Motil Cytoskeleton* **42**, 149–161 (1999).

34. Kirkman-Brown, J. C. & Smith, D. J. Sperm motility: is viscosity fundamental to progress? *Mol Hum Reprod* **17**, 539–544 (2011).

35. Okuno, M. & Hiramoto, Y. Direct Measurements of the Stiffness of Echinoderm Sperm Flagella. *Journal of Experimental Biology* **79**, 235–243 (1979).

36. Durlofsky, L., Brady, J. F. & Bossis, G. Dynamic simulation of hydrodynamically interacting particles. *J Fluid Mech* **180**, 21 (1987).

37. Swan, J. W. & Brady, J. F. Simulation of hydrodynamically interacting particles near a no-slip boundary. *Physics of Fluids* **19**, 113306 (2007).

38. Gaffney, E. A., Ishimoto, K. & Walker, B. J. Modelling Motility: The Mathematics of Spermatozoa. *Front Cell Dev Biol* **9**, (2021).

39. Lauga, E. & Powers, T. R. The hydrodynamics of swimming microorganisms. *Reports on Progress in Physics* **72**, 96601 (2009).

40. Katz, D. F., Blake, J. R. & Paveri-Fontana, S. L. On the movement of slender bodies near plane boundaries at low Reynolds number. *J Fluid Mech* **72**, 529 (1975).

41. Beta, C. & Kruse, K. Intracellular Oscillations and Waves. *Annu Rev Condens Matter Phys* **8**, 239–264 (2017).

42. Grill, S. W., Kruse, K. & Jülicher, F. Theory of Mitotic Spindle Oscillations. *Phys Rev Lett* **94**, 108104 (2005).

43. Jülicher, F. & Prost, J. Cooperative Molecular Motors. *Phys Rev Lett* **75**, 2618–2621 (1995).

44. Lin, J. & Nicastro, D. Asymmetric distribution and spatial switching of dynein activity generates ciliary motility. *Science (1979)* **360**, (2018).

45. Lindemann, C. B. & Lesich, K. A. Flagellar and ciliary beating: the proven and the possible. *J Cell Sci* **123**, 519–528 (2010).

46. King, S. M. Integrated control of axonemal dynein AAA+ motors. *J Struct Biol* **179**, 222–228 (2012).

47. Ling, F., Guo, H. & Kanso, E. Instability-driven oscillations of elastic microfilaments. *J R Soc Interface* **15**, 20180594 (2018).

48. Sartori, P., Geyer, V. F., Howard, J. & Jülicher, F. Curvature regulation of the ciliary beat through axonemal twist. *Phys Rev E* **94**, 042426 (2016).

49. Gadêlha, H. & Gaffney, E. A. Flagellar ultrastructure suppresses buckling instabilities and enables mammalian sperm navigation in high-viscosity media. *J R Soc Interface* **16**, 20180668 (2019).

50. Ishimoto, K. & Gaffney, E. A. A study of spermatozoan swimming stability near a surface. *J Theor Biol* **360**, 187–199 (2014).

51. Fily, Y., Subramanian, P., Schneider, T. M., Chelakkot, R. & Gopinath, A. Buckling instabilities and spatio-temporal dynamics of active elastic filaments. *J R Soc Interface* **17**, 20190794 (2020).

52. Sangani, A. S. & Gopinath, A. Elastohydrodynamical instabilities of active filaments, arrays, and carpets analyzed using slender-body theory. *Phys Rev Fluids* **5**, 83101 (2020).

53. Zhang, T. & Goldman, D. I. The effectiveness of resistive force theory in granular locomotion. *Physics of Fluids* **26**, 101308 (2014).

54. Sakakibara, H. M., Kunioka, Y., Yamada, T. & Kamimura, S. Diameter Oscillation of Axonemes in Sea-Urchin Sperm Flagella. *Biophys J* **86**, 346–352 (2004).

55. Piperno, G. & Luck, D. J. L. Outer and inner arm dyneins from flagella of Chlamydomonas reinhardtii. *Cell Motil* **2**, 95–99 (1982).

56. Lindemann, C. B. Structural-Functional Relationships of the Dynein, Spokes, and Central-Pair Projections Predicted from an Analysis of the Forces Acting within a Flagellum. *Biophys J* **84**, 4115–4126 (2003).

57. Yazdan Parast, F. *et al.* Viscous Loading Regulates the Flagellar Energetics of Human and Bull Sperm. *Small Methods* (2023) doi:10.1002/smtd.202300928.

58. Powers, T. R. Dynamics of filaments and membranes in a viscous fluid. *Rev Mod Phys* **82**, 1607–1631 (2010).

59. Hines, M. & Blum, J. J. Bend propagation in flagella. I. Derivation of equations of motion and their simulation. *Biophys J* **23**, 41–57 (1978).

60. Schoeller, S. F., Townsend, A. K., Westwood, T. A. & Keaveny, E. E. Methods for suspensions of passive and active filaments. *J Comput Phys* **424**, 109846 (2021).

61. Wajnryb, E., Mizerski, K. A., Zuk, P. J. & Szymczak, P. Generalization of the Rotne–Prager–Yamakawa mobility and shear disturbance tensors. *J Fluid Mech* **731**, R3 (2013).

62. Lighthill, J. Flagellar Hydrodynamics. *SIAM Review* **18**, 161–230 (1976).

63. Gu, N.-H., Zhao, W.-L., Wang, G.-S. & Sun, F. Comparative analysis of mammalian sperm ultrastructure reveals relationships between sperm morphology, mitochondrial functions and motility. *Reproductive Biology and Endocrinology* **17**, 66 (2019).

## Acknowledgements

This work was supported by a Discovery Project Grant (DP190100343) from the Australian Research Council.

## Author contributions

S.V., R.P. and R.N. designed the research. S.V. and R.P. developed the mathematical model and analysis. S.V. implemented the code and performed the simulations. F.P. and R.N. designed the experiments. F.P. performed the experiments. S.V. analyzed data and wrote the manuscript. S.V., F.P., R.P. and R.N. edited the manuscript.

## Competing financial interests

The authors declare no competing interests.

## Materials & Correspondence.

Correspondence should be addressed to R.P. (email: Prabhakar.Ranganathan@monash.edu).